# Journal of Materials Chemistry A



**PAPER** 

View Article Online
View Journal | View Issue



Cite this: J. Mater. Chem. A, 2024, 12, 8940

# Giant Stark effect assisted radio frequency energy harvesting using atomically thin earth-abundant iron sulphide (FeS<sub>2</sub>)†

Karthik R.,<sup>a</sup> Appu Kumar Singh,<sup>a</sup> Shreyasi Das,<sup>b</sup> Suman Sarkar,<sup>c</sup> Tarun Kumar Kundu, <sup>Da</sup> Swastik Kar, <sup>Dd</sup> P. R. Sreeram <sup>b\*a</sup> and Chandra Sekhar Tiwary <sup>b\*a</sup>

The advancement in two-dimensional (2D) materials has led to the development of new charging methods in portable and wearable electronic devices. However, their charging methods are still confined to contact/ wired mode. Radio Frequency (RF) energy harvesting exhibits potential for extracting electrical power from the environment, benefiting from its limitless ambient availability and extended power transfer capabilities. This paper demonstrates the fabrication of an RF energy harvesting device using liquid phase exfoliated atomically thin earth-abundant pyrite ore (iron sulfide (FeS<sub>2</sub>)). Owing to pyrite's unique semiconductor properties such as a very small narrow band gap (0.8 eV) and high carrier mobility (360 cm<sup>2</sup> V<sup>-1</sup> s<sup>-1</sup>), it is possible to make a Schottky junction with a metal electrode. Hence, we fabricated a Schottky device employing a Ti/2D-FeS<sub>2</sub>/ITO configuration using drop casting methods. Electrical measurements reveal that the device has a low turn-on voltage of 0.18 V and a low Schottky barrier height of 0.14 eV. To substantiate the role of 2D-FeS2, density functional theory (DFT) studies were performed revealing the impact of the Giant Stark Effect (GSE) in lowering the bandgap of 2D FeS<sub>2</sub>. This insidious phenomenon of GSE in 2D-FeS<sub>2</sub> makes it an ideal material of choice for RF energy harvesting applications. The device we fabricated functions within the commercial frequency modulation broadband range and extends seamlessly into the very high-frequency radio spectrum. It generated a 1.5 V output voltage using commercial FM broadband frequencies, sufficient for charging a 1.5 F supercapacitor. Subsequent experimentation with a handheld walkie-talkie demonstrated that the device could achieve a maximum voltage of 3.5 V within the one-meter range, exhibiting an efficiency of 30%. The implications of this discovery suggest that 2D-FeS2-based wireless energy-powered portable devices hold promise for healthcare/biomedical device applications, energy harvesting in remote areas, and regions affected by floods or natural disasters

Received 20th December 2023 Accepted 4th March 2024

DOI: 10.1039/d3ta07906f

rsc.li/materials-a

# 1 Introduction

The progress in electronics has given rise to the emergence of portable and wearable smart devices. However, their dependence on wired charging poses limitations such as immobility, safety concerns, costs, and scalability issues. In such contexts, wireless energy harvesting emerges as a promising alternative.

Radiofrequency (RF) energy harvesting, in particular, is gaining traction with the rapid expansion of wireless telecommunication devices like Wi-Fi, cell phone towers, and radio broadcast stations. This system can capture RF signals from these sources and convert them into useable direct current (DC) without requiring an external power source.1 At the core of an RF energy harvester lies the semiconductor responsible for rectifying highfrequency radio waves. High carrier mobility Schottky devices are typically necessary to ensure efficient high-frequency cut-off operation. RF energy harvesting has been shown to work on rigid substrates like silicon and group III-V compounds.2 Nevertheless, modifying the electronic characteristics of these materials, such as electron affinity, carrier mobility, and work function, may prove challenging. Consequently, their substantial size restricts their applicability to flexible devices. Graphene and other two-dimensional (2D) materials, such as tellurides,3 metal oxides,4 and transition metal dichalcogenides (TMDC),5 have received significant attention for their potential

<sup>&</sup>lt;sup>a</sup>Department of Metallurgical and Materials Engineering, Indian Institute of Technology Kharagpur, West Bengal 721302, India. E-mail: sreerampunam@metal.iitkgp.ac.in; chandra.tiwary@metal.iitkgp.ac.in

<sup>&</sup>lt;sup>b</sup>School of Nano Science and Technology, Indian Institute of Technology Kharagpur, West Bengal 721302, India

Department of Materials Engineering, Indian Institute of Technology Jammu, Jammu 181221, India

<sup>&</sup>lt;sup>d</sup>Department of Physics, Quantum Materials and Sensing Institute, Department of Chemical Engineering, Northeastern University, Boston, Massachusetts 02115, USA † Electronic supplementary information (ESI) available. See DOI: https://doi.org/10.1039/d3ta07906f

applications in sensing and energy harvesting.6 Among them, TMDC,5 metal oxides7 and tellurides3 have been reported as potential candidates for sensing, energy storage and energy harvesting applications. 2D materials have been wellestablished for piezoelectric, triboelectric and flexoelectric applications.8 Altering the thickness of 2D materials allows for tuning properties like carrier mobility, work function, and band gap.9

Recent studies have showcased RF energy harvesting utilising well-known van der Waals (vdW) materials such as MoS2,10 WSe2,11 and MoSe2.12 Vertical Schottky devices were fabricated using mechanical exfoliation and atomic layer deposition methods. However, the associated costs of device fabrication and material processing complexity have hindered their practical application. An intriguing alternative has emerged in the form of RF energy harvesting using naturally available lead sulphide (PbS).13 Obtaining a lower Schottky barrier and higher carrier mobility is of utmost importance in radio frequency applications. A lower barrier minimises energy loss, while higher mobility guarantees a strong response at high frequencies.14 The device should have a low turn-on voltage and low series resistance for enhanced sensitivity. Most devices using the above materials have a high turn-on voltage and series resistance, limiting the efficiency since the received RF power will be relatively low. Developing a device with a low turn-on voltage without additional electronic components is advantageous for a miniaturised energy harvesting system.15 In addition, given the environmental implications associated with the use of materials like selenides and lead, there is a necessity for exploring alternative eco-friendly materials to pave the way for a sustainable future. One such material of interest is iron sulfide (FeS2)/pyrite.

FeS<sub>2</sub> exhibits two polymorphic phases, pyrite and marcasite. Among them pyrite also known as Fool's gold due to its paleyellow appearance is the most abundant sulphide ore found in the earth's crust. 16,17 They are usually found along with other sulphides or oxides in sedimentary and metamorphic rocks making them the best choice for environment-friendly, inexpensive and readily available material. Pyrite is primarily used for the production of sulphur dioxide for the paper industry and also for sulphuric acid production for fertilizers. Beyond its primary applications, researchers have also used pyrite for energy applications due to its unique semiconducting nature. Pyrite has a small band gap of (0.8-0.95 eV) and a high electron carrier mobility of 360 cm<sup>2</sup> V<sup>-1</sup> s<sup>-1</sup>. It's crystal structure has a close resemblance to sodium chloride, where iron and sulphur irons are replaced with sodium and chloride ions. FeS2 nanoparticles are employed in diverse applications, including battery electrodes,18 catalytic processes,19 and optical applications.20 They have synthesised such nanoparticles using a variety of physical and chemical methods such as spray pyrolysis, template-directed methods and solvothermal methods by employing chemical precursors. These methods are often tedious and most importantly they are missing the opportunity to explore the natural properties of earth-abundant pyrite. Moreover, it's difficult to control the stoichiometry and crystallinity of the products by using these methods and end up

getting unwanted by-products such as FeS and Fe3S4. It is noteworthy to say that researchers have reported the synthesis of quantum dots, and nanowires using FeS2 however very few have reported the synthesis of 2D-FeS2. Theoretical studies have shown that the exfoliation energy of FeS<sub>2</sub> (58 meV per atom) is similar to that of exfoliation energy for layered TMDs such as WS<sub>2</sub> (56 meV per atom) and MoS<sub>2</sub> (72 meV per atom) indicating the possibility of synthesising 2D-FeS<sub>2</sub> nanoparticles by liquid phase exfoliation (LPE).21

In this work, we employed the LPE method for synthesising 2D-FeS<sub>2</sub> using the ultrasonic probe sonication method. Isopropyl alcohol is used as the exfoliating medium because of its high boiling point (82.5 °C) and low toxicity when compared to other solvents such as NMP. In addition to that the obtained nanoparticles dispersion were easily dried in ambient conditions without affecting the chemistry of the material. Moreover, the scale of production via the LPE method is guite high when compared to methods like mechanical exfoliation and chemical vapour deposition (CVD) methods. The structural and morphological studies of the obtained 2D-FeS2 were analysed using microscopic and spectroscopic studies. Pyrite being a narrow bandgap semiconductor, it is possible to make a Schottky device by simply making a metal contact which can act like a small signal diode for radiofrequency applications. A device for RF energy harvesting was thus fabricated using the drop-casting method under ambient conditions, employing a Ti/2D-FeS<sub>2</sub>/ITO configuration. The drop-casting method is more profitable and easier because the dispersion containing 2D nanoparticles can be coated on any substrate of interest. Whereas in methods like mechanical exfoliation and CVD, it is tedious to transfer the material to the substrate and there is a need for specific substrates and conditions for growing the material which is costly and time-consuming. A variety of electrical measurements of the device showed a very low turn-on voltage of 0.18 V which is ideal for radio frequency applications. RF studies showed the device's performance in frequency modulation (FM) broadband and very high-frequency (VHF) bands. In addition to experimental studies, we also performed density functional theory (DFT) studies revealing the existence of Giant Stark Effect (GSE) analogous to the conventional Stark effect observed in atomic orbitals in 2D-FeS2 layers,22 which is one of the major reasons for RF response of 2D-FeS2. The alteration in the electronic band structure of the material induced through the GSE sheds new light on RF energy harvesting using 2D materials.

#### 2 Result and discussion

Fig. 1 illustrates the schematic depiction of the 2D-FeS<sub>2</sub> synthesis process employing the liquid-phase exfoliation technique, followed by the fabrication of an RF energy harvesting device designed for diverse applications. The phases present in bulk and the exfoliated samples were analysed and compared using XRD analysis, depicted in Fig. 2a. Cubic FeS2 crystals have the space group  $Pa\bar{3}$  and the lattice parameters a = b = c = 5.39Å, corresponding to the ICSD 53935. X-ray diffraction analysis of bulk FeS2 reveals an intense peak in the (211) plane, while that

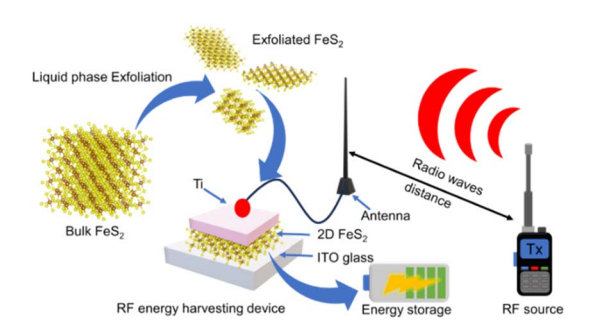


Fig. 1 Schematic representation of exfoliation of bulk to 2D-FeS $_2$  and its application for RF energy harvesting.

of an exfoliated sample lies in the (200) plane. The peak shift towards lower  $2\theta$  in the exfoliated sample is due to lattice expansion in the crystal. This increase in lattice expansion is an

indication of the formation of FeS2 nanoparticles. No other phases were detected from XRD analysis. AFM analysis was performed to verify the thickness of the exfoliated FeS2. The thickness profile and AFM image of the FeS2 sample are shown in Fig. 2b. From the AFM analysis, the obtained sample has an average thickness of 0.62 nm (1-2 layers), which justifies the formation of 2D-FeS2. Analyses were performed to investigate the morphology of the 2D-FeS2 to understand the obtained nanoparticles better. From Fig. 2c, the obtained 2D-FeS2 has a more irregular flake-like morphology with an average lateral length of  $\sim$ 0.9  $\mu$ m. A deep understanding of the 2D flakes was analysed using HRTEM. From Fig. 2d it is observed that there is an even arrangement of atoms. The zoomed-in HRTEM (Fig. 2e) image shows a precise arrangement of atoms along the (221) plane, and the lattice spacing was found to be 1.79 nm, which is in good agreement with the (221) plane, as seen in the XRD analysis of 2D-FeS2. The SAED pattern of FeS2 nanocrystals is

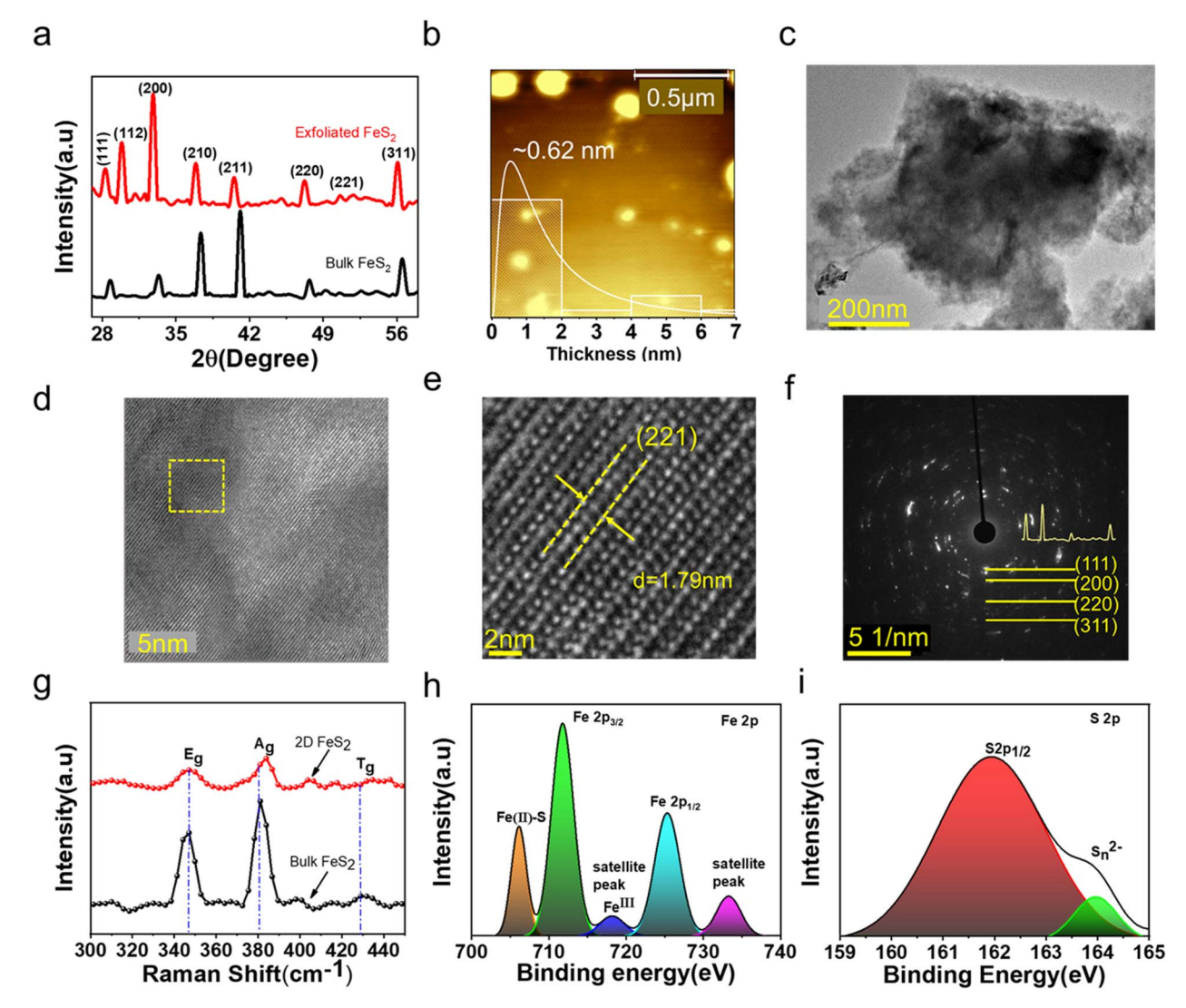


Fig. 2 (a) XRD pattern of bulk and exfoliated  $FeS_2$ , (b) AFM image with thickness profile of 2D- $FeS_2$  (c and d) bright field HRTEM image of 2D- $FeS_2$ , (e) zoomed in view of marked section from (d), (f) SAED pattern of 2D- $FeS_2$  showing (111) (200) (220) (311) planes, (g) Raman spectra of bulk and 2D- $FeS_2$  with various vibrational modes and (h and i) XPS spectra of 2D- $FeS_2$  showing Fe 2p and S 2p binding energy plots.

depicted in Fig. 2f. The circular ring pattern with indexing and XRD analysis supports the overall polycrystalline nature of the obtained 2D-FeS2.

The vibrational states of bulk and 2D-FeS2 were analysed using Raman spectroscopy. Fig. 2g shows that the Raman spectra of both bulk and 2D-FeS2 show the double regeneration (E<sub>g</sub>), symmetric mode (A<sub>g</sub>), and stretching (T<sub>g</sub>) modes. The E<sub>g</sub> mode corresponds to  $S_2$  liberation, and  $A_{\rm g}$  corresponds to the in-phase stretching vibration of the S-S dimer. The  $T_{\rm g}$  mode indicates coupled liberation and stretching modes.23,24 In the case of 2D-FeS<sub>2</sub>, a peak position to the right is shifted by 2 cm<sup>-1</sup>. This is probably due to the generation of compressive strain in the material due to exfoliation. No other vibrational modes are present, indicating the absence of other phases. The chemical oxidation states of 2D-FeS2 were analysed using XPS. Fig. 2(h and i) shows XPS plots of Fe 2p and S 2p. The Fe 2p is further resolved to Fe 2p<sub>1/2</sub> (711.6 eV) and Fe 2p<sub>3/2</sub> (725 eV).<sup>25</sup> In addition to this, satellite peaks are observed at binding energies of 718.2 eV and 733.2 eV. The peak at 706.2 eV indicates Fe(II)-S. In the case of S 2p, a broad peak at 162 eV corresponds to the S (2p<sub>1/2</sub>) core level of S<sup>2+</sup> associated with the formation of FeS<sub>2</sub>.<sup>26</sup> The absence of any additional peaks indicates the purity of the

sample after exfoliation. Hence, the above studies confirm the formation of stable 2D FeS<sub>2</sub>

Electrical studies were performed to understand the electronic nature of 2D-FeS2. Hall effect measurements elucidated the semiconducting nature of 2D-FeS2, revealing it as a p-type semiconductor with a carrier concentration of  $3.74 \times 10^{18}$ cm<sup>-3</sup> and carrier mobility of 5.81 cm<sup>2</sup> V<sup>-1</sup> s<sup>-1</sup>. Additional electrical studies were conducted to determine the formation of the Schottky diode. Carrier mobility is one crucial factor determining Schottky device characteristics, such as highfrequency response and operating speed. Fig. 3(a and b) depicts the device configuration graphically and pictorially. Fig. 3c shows the optical image of the Ti metal contact with a diameter of 1 mm and a contact area of 0.785 mm<sup>2</sup>. Fig. 3d shows a cross-sectional SEM image revealing the coating thickness of  $\sim$ 25 µm by drop-casting 2D-FeS<sub>2</sub> onto ITO-coated glass. An FESEM image of 2D-FeS2 with particle size distribution is given in ESI Fig. S2.† The coating comprises FeS<sub>2</sub> nanoparticles with an average particle size of 260 nm. The work function of FeS<sub>2</sub> (5.45 eV) is higher than that of Ti (4.33 eV), which satisfies the conditions necessary for the establishment of a Schottky junction  $(\Phi_{\text{FeS}_2} > \Phi_{\text{Ti}}).^{27,28}$  Current-voltage (I-V)

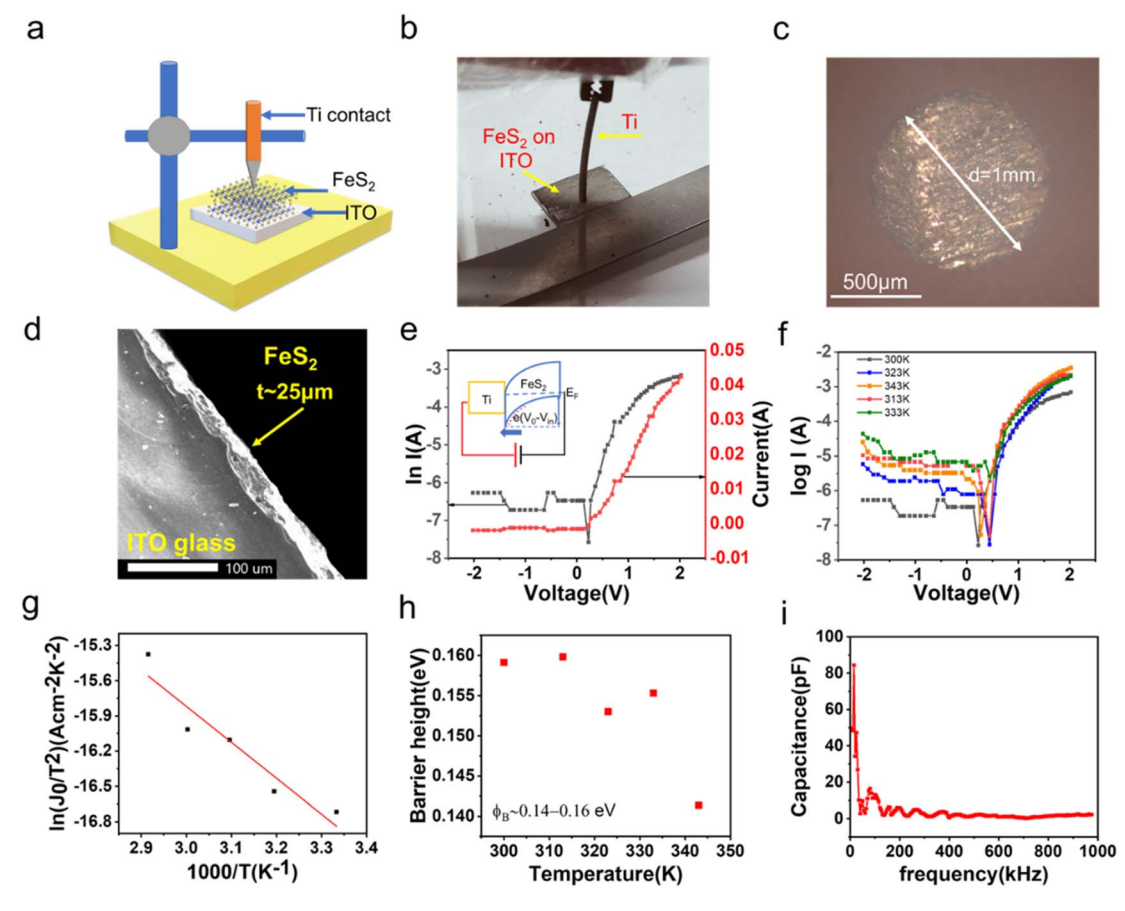


Fig. 3 (a) Graphical image of Ti/2D-FeS<sub>2</sub>/ITO device setup; (b) pictorial image of device setup showing Ti/2D-FeS<sub>2</sub>/ITO contacts; (c) optical image of Ti metal contact; (d) SEM cross-sectional image showing the thickness of FeS<sub>2</sub> coating; (e) current-voltage characteristics of Ti/2D-FeS<sub>2</sub>/ITO device; and (f) temperature-dependent I-V characteristics of Ti/2D-FeS<sub>2</sub>/ITO device with inset showing energy band diagram; (g) Richardson plot of  $\ln(J_0/T^2 versus 1000/T)$  (h) barrier height versus temperature plot (i) junction capacitance measurement at various frequencies of Ti/2D-FeS2/ITO device.

analyses were conducted to substantiate the Schottky characteristics of both bulk and 2D-FeS2 devices. Bulk FeS2 shows a linear behaviour with a small rectifying nature, which is not ideal for rectifier applications (Fig. S3†). Fig. 3e depicts the I-V characteristics of the Ti/2D-FeS2/ITO device. The nonlinear increase in the current during the forward bias operation signifies rectifying behaviour, confirming the formation of a Schottky junction. The device has an on-off ratio of 10<sup>5</sup> cycles, ideal for high-frequency signal and RF applications. In addition to the aforementioned experiments, we have also conducted measurements on the thickness-dependent I-V characteristics of 2D-FeS<sub>2</sub>. Remarkably, as the thickness increases, the turn-on voltage shows a corresponding increase, and intriguingly, the device ceases to display any rectification behaviour at higher thicknesses. The thickness-dependent I-V characteristics have been depicted in ESI Fig. S4.† Consequently, we have opted for a 25 µm thickness FeS2 coating for further measurements for better rectification. Temperature-dependent I-V studies (Fig. 3f) were also performed to calculate Schottky barrier height from the Richardson plot (Fig. 3g). The Schottky barrier height is calculated using the following equation13

$$\Phi_{\rm B} = \frac{kT}{q} \ln \left( \frac{A^* A T^2}{I_0} \right) \tag{1}$$

where  $\Phi_{\rm B}$  is the barrier height, k is the Boltzmann constant, T is the temperature, q is the charge of electrons,  $A^*$  is the Richardson constant, A is the area of cross-section, and  $I_0$  is the reverse saturation current. The calculated barrier height falls in the range of 0.14-0.16 eV, as shown in Fig. 3h. Also, it is observed that as temperature increases, the barrier height lowers, which could be due to the tunnelling of thermally activated electrons into the semiconductor depletion region. The reduction in the metal-semiconductor junction contributes to a decrease in the Schottky barrier height, with the observed low values attributed notably to Fermi-level pinning at the interfaces of Ti/2D-FeS2.29 Theoretically, a lower Schottky barrier height is recommended for RF applications, as the lower energy of radio waves facilitates the easy excitation of electrons, enabling efficient current flow.13 The capacitance of the device is also analysed to assess the impact of capacitance on the device's performance. Fig. 3i shows capacitance values at various frequencies, and at higher frequencies, the junction capacitance remains almost constant with an average capacitance of  $\sim$ 3 pF.

By establishing a Schottky junction, we describe an experimental demonstration of energy harvesting employing a fabricated device that can wirelessly capture and convert RF signals to appropriate electrical energy. Fig. 4(a and b) shows the schematic representation and photographic image of the lab-made experimental setup. A lab-made RF setup consists of an RF signal generator, RF amplifier, DC source and a dipole antenna. A separation distance of 40 cm was maintained between the transmitter and receiver antennas, with the recording of input and output waveforms accomplished using a dual-channel oscilloscope. Our interest is to check RF response in FM broadband frequencies. Therefore, we opted for two FM broadband frequencies, namely 88 MHz and 94 MHz,

with an amplitude of 0.8 V and RF power of 20 dBm (100 mW), as they are presently not used by our nearby FM stations. Fig. 4c and d shows the input and output waveform of the RF signal to the device. It is visible that the output waveforms appear in a positive cycle, indicating the rectification behaviour of the device. As frequency increased, the ripples in the output waveform decreased. This observation aligns with the inverse relationship between frequency and ripple amplitude, suggesting a smoother waveform at higher frequencies. Ripples are expected to persist in low frequencies as no supplementary RC circuit has been incorporated. All the measurements were done at room temperature conditions. These results justify the Schottky diode behaviour of Ti/2D-FeS<sub>2</sub>/ITO devices.

Subsequently, the charging of a supercapacitor utilising an RF energy harvesting device in the FM broadcast band is illustrated, as depicted in Fig. 4e. We connected a supercapacitor of 1.5 F to the output of the device to store the voltage generated from the device. A load (LED) is connected across the capacitor for the discharging study. The device received an RF input at 94 MHz with a signal amplitude of 2 V and RF power of 20 dBm (100 mW) for 20 seconds, leading to the recording of the resulting stored voltage  $(V_{st})$ , as illustrated in Fig. 4f. The RF input signal turned off after 20 seconds, and it stopped charging the capacitor. Remarkably, the supercapacitor attained a voltage storage level of 2 V within 20 seconds, and this capacity can be further augmented by prolonging the duration of RF charging and increasing RF input power. A gradual decrease in the voltage after turning off the RF is due to the discharging of the capacitor through the load. This shows the potential of wireless RF charging using Ti/2D-FeS2/ITO devices. ESI Video V1† shows the charging and discharging of a supercapacitor when an RF signal is applied. Based on these findings, we infer that FeS<sub>2</sub> is a promising material for RF-powered supercapacitor charging.

By confirming RF studies in FM broadband and expecting further high-frequency response, we performed an in situ demonstration of wireless RF energy harvesting using a handheld walkie-talkie. Fig. 5(a and b) shows the schematic and pictorial representation of the experimental setup for demonstrating RF energy harvesting. A handheld walkie-talkie of 200 mW power with operating frequencies of 130-176 MHz was used as the RF source. Fig. 5c illustrates the input and output waveforms at 150 MHz, revealing a distinct DC behaviour in the output signal. Hence, we proceeded to investigate RF energy harvesting in the above frequencies. The output voltage and power from the device is measured across a resistor  $R_{\rm L}$  220  $\Omega$  at various distances and frequencies, as shown in Fig. 5(d and e). It is observed that the voltage and power generated decrease with an increase in distance, which is a general observation of the attenuation of electromagnetic waves with distance. From power calculations, the efficiency of the device was calculated at various frequencies, as shown in Fig. 5e. The ratio of power generated to power input was used to calculate efficiency. The calculations indicate that the device exhibits an efficiency of approximately 30% at 155 MHz, with a notable decrease in efficiency observed at 170 MHz. By using the measured values of

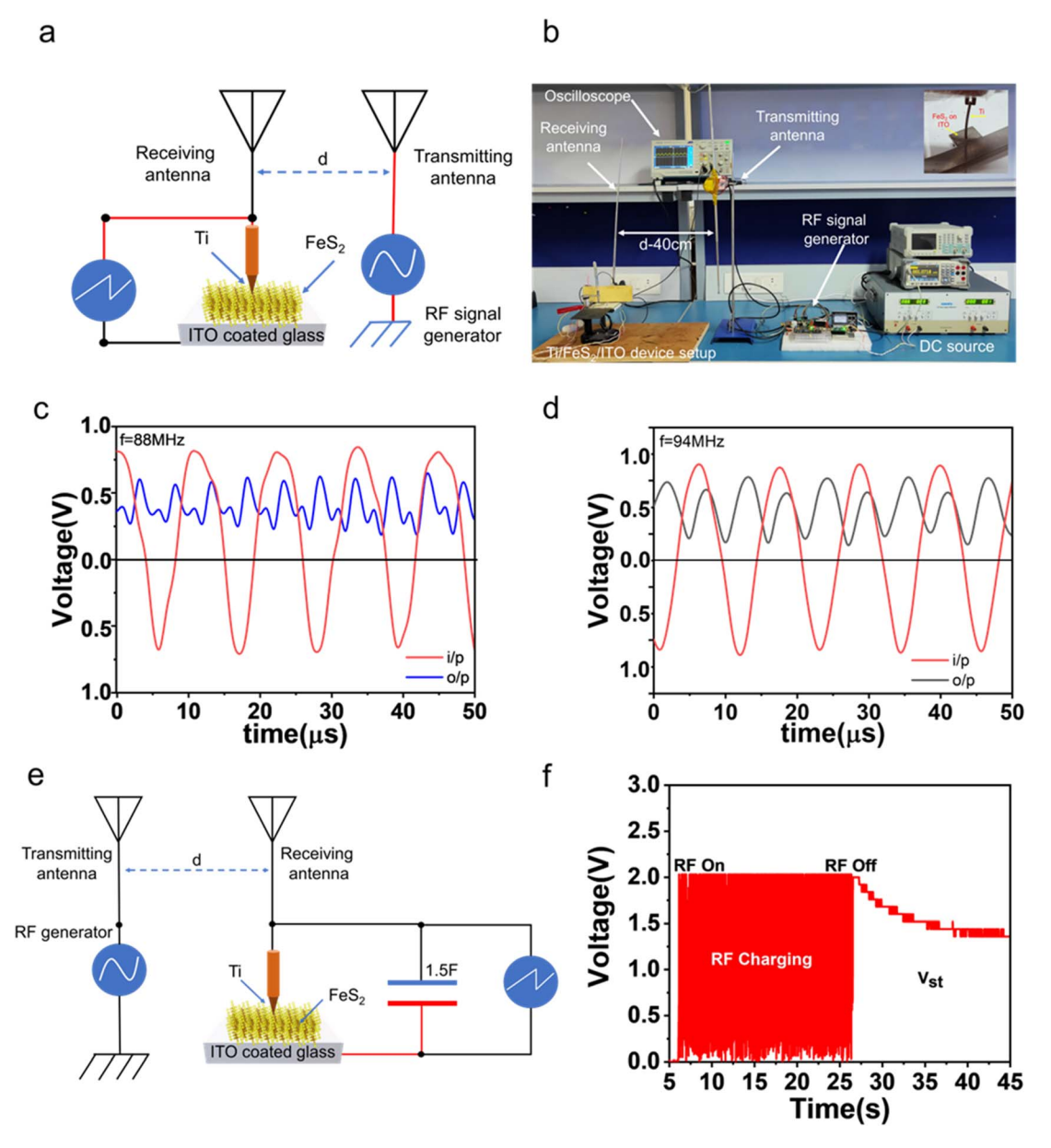


Fig. 4 (a) Schematic representation of the experimental setup showing Ti/2D-FeS<sub>2</sub>/ITO device; (b) photographic image of the experimental setup with inset showing Ti/2D-FeS<sub>2</sub>/ITO contacts (c and d) half wave rectification behaviour of the device with FM broadcast frequencies 88 MHz and 94 MHz. Here, red indicates the input signal, and blue and black indicate the output signal (e) schematic representation of wireless charging of supercapacitor using  $Ti/2D-FeS_2/ITO$  device (f) RF charging and discharging plots of the supercapacitor  $(V_{st}$ -stored voltage).

junction capacitance  $C_i$  (3 pF) and resistance  $R_s$  (310  $\Omega$ ), the cutoff frequency is calculated using the following formula.

$$f_{\rm cutoff} = \frac{1}{2\pi R_{\rm s} C_{\rm j}} \tag{2}$$

The obtained cut-off frequency value is ~171 MHz, which matches our experimental studies. So, any further increase in frequency may not produce voltage from the device, limiting its performance up to 170 MHz. Such a cut-off frequency is desirable because most ambient RF energy sources will have frequencies in a 3-300 MHz domain. The efficiency of the device can be extended by adding a suitable impedance-matching network and

proper antennas. The ESI Video V2† demonstrates energy harvesting from a handheld walkie-talkie by connecting an LED across the fabricated device. Inorder to verify that the Schottky junction is formed between Ti and 2D-FeS2, we fabricated a Ti/ ITO device without 2D-FeS2 and measured IV and RF responses. We found no formation of a Schottky junction and no RF response in the absence of FeS<sub>2</sub>. ESI Fig. S5† shows the I-V and RF responses of the Ti/ITO configuration.

The electronic characteristics of 2D-FeS2 hold considerable influence over device properties, notably the turn-on voltage  $(V_t)$ and barrier height  $(\Phi_B)$ . These parameters, crucial for device performance, are inherently linked to electronic properties such as band gap and electron affinities. To better understand these

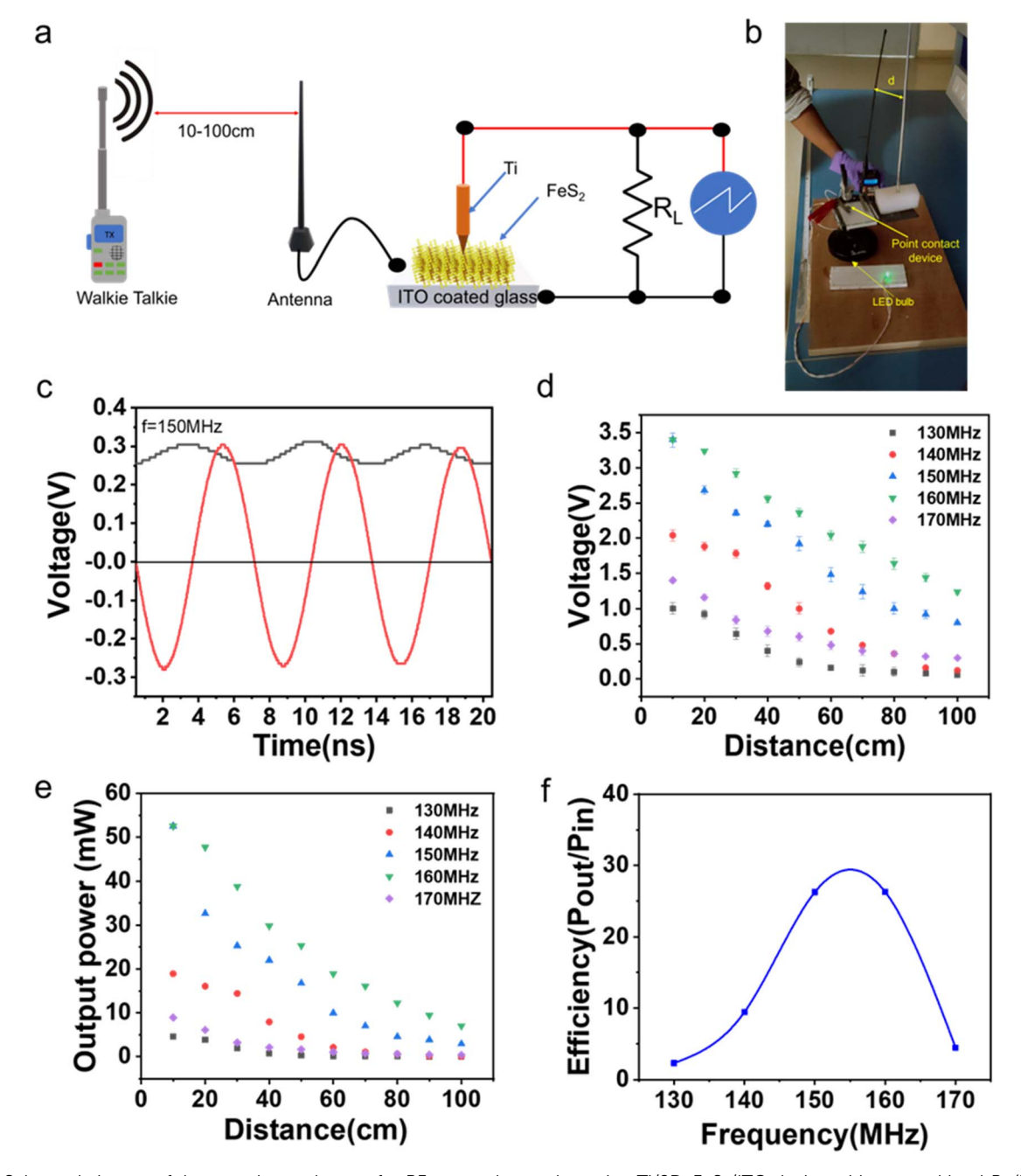


Fig. 5 (a) Schematic image of the experimental setup for RF energy harvesting using Ti/2D-FeS<sub>2</sub>/ITO device with external load  $R_L$  (b) pictorial representation of experimental setup; (c) input and output waveforms of RF signal given to device at 150 MHz (d) output voltage versus distance plots at various frequencies, (e) output voltage versus distance plots at various frequencies and (f) efficiency versus frequency plots at various frequencies.

complex electronic properties and how they affect device behaviour, we therefore performed Density Functional Theory (DFT) studies on bulk and 2D-FeS2. After variable cell relaxation of FeS<sub>2</sub>, bulk FeS<sub>2</sub> was determined to have a cubic structure with a = 5.361 Å, and  $Pa\bar{3}$  space group. Iron atoms occupy an octahedral position, and sulfur occupies a tetrahedral position, similar to the experimental observations, as shown in Fig. 6a. In 2D-FeS<sub>2</sub> with a (1 0 0) plane, the core of the crystal structure is similar to that of bulk, while the edge atoms are crystallised in tetrahedron iron atoms, as depicted in Fig. 6b. A stable 2D-FeS2 crystal structure shows compressive lattice strain, with lattice parameters a = 5.3167 Å, and b = 5.4484 Å, which was also observed in experiment results. Calculated vibration spectroscopy for the obtained crystal structure also shows no imaginary values, which confirms its dynamic stability.

Spectroscopic analyses were conducted to establish a correlation between the DFT studies of FeS<sub>2</sub>. Experimental UV-vis spectroscopy results confirm a decrease in the optical band gap from 2.5 eV (bulk) to 1.3 eV (2D). Notably, this experimental finding is consistent with the optical band gap of 2D-FeS2

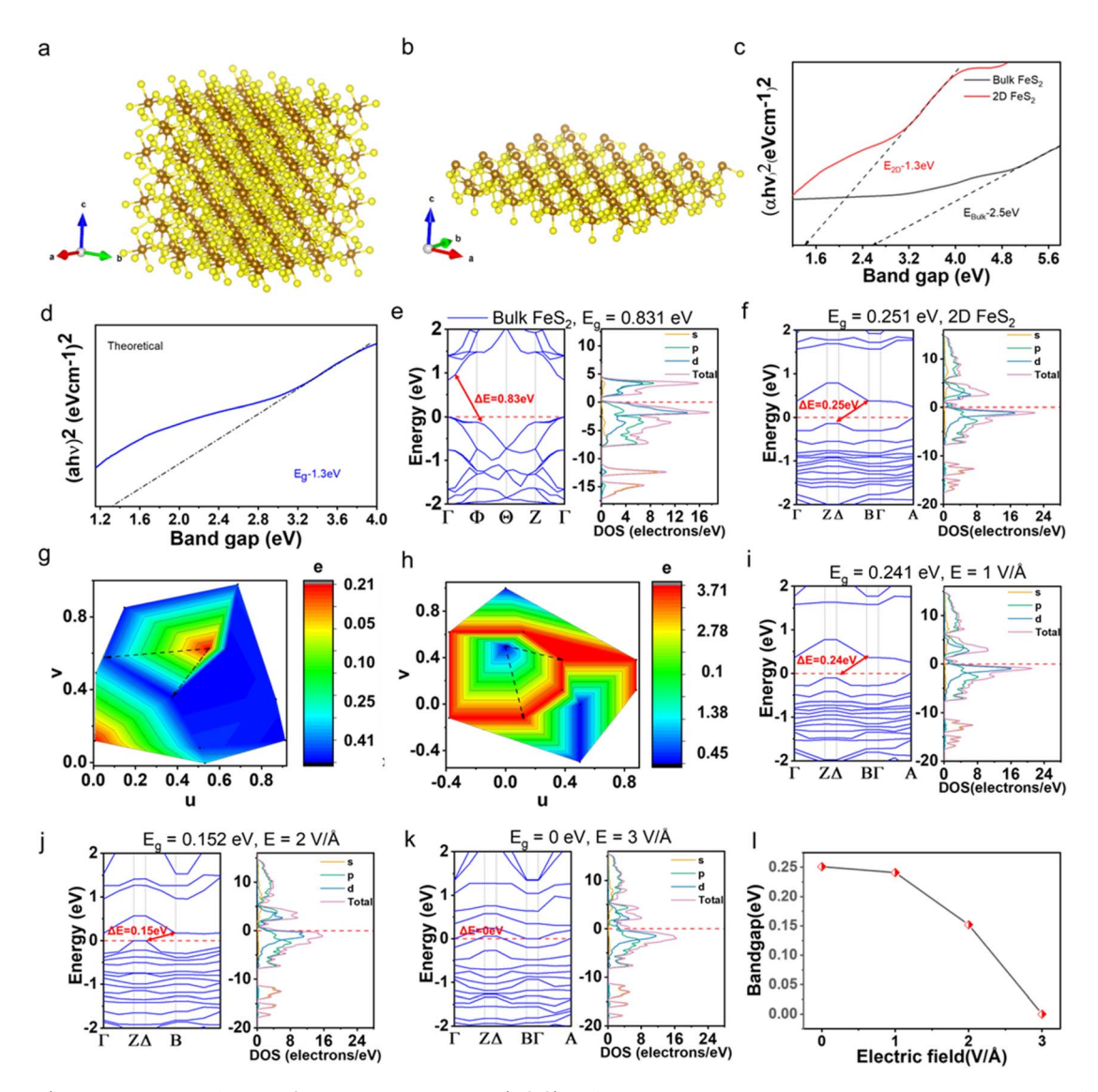


Fig. 6 (a and b) Representation of bulk FeS<sub>2</sub> crystal structure and (1 0 0) surface; iron atoms representing in brown colour, and sulfur in yellow colour; (c) optical bandgap (experimental) (d) optical bandgap (theoretical); (e) band structure of bulk showing minima at  $\Gamma$  point for 0.831 eV (f) band structure of (1 0 0) surface showing minima at an end for 0. 241 eV; (g and h) charge distribution contour graph of (g) bulk (h) 2D (1 0 0) plane; (i–k) effect of electric field variation on FeS<sub>2</sub>(1 0 0) surface band structure at  $E = 1 \text{ V Å}^{-1}$ ,  $E = 2 \text{ V Å}^{-1}$  and  $E = 3 \text{ V Å}^{-1}$  and (l) variation of bandgap with electric field

determined through DFT analysis, as illustrated in Fig. 6(c and d). This alignment underscores the agreement between theoretical calculations and experimental observations, enhancing our understanding of the electronic properties of FeS<sub>2</sub>. From the DOS plot, the electronic bandgap of bulk and 2D-FeS2 is 0.831 eV and 0.251 eV, respectively, as depicted in Fig. 6(e and f). The polarisation mechanism in bulk and 2D-FeS2 is shown in Fig. 6(g and h). Bulk FeS<sub>2</sub> shows an even distribution of the charge because of the cubic crystal symmetry, whereas 2D shows the localisation of the charge. Considering an electric dipole,  $\vec{p} = q_{\text{net}} \vec{d}$ , where  $q_{\text{net}}$  is the net charge between two atoms, and d is the distance separated. In bulk FeS<sub>2</sub>,  $\overline{P_1}$  and  $\overline{P_2}$  are two electric dipoles (dashed lines) in two different directions, but the resultant is zero due to the cubic crystal symmetry. But in the case of 2D-FeS<sub>2</sub>, the resultant is non-zero,

 $\overrightarrow{P_3}$  and  $\overrightarrow{P_4}$  has values in 1.86 eÅ and 0.744 eÅ in the x-direction. This localisation effect and anisotropic charge surface create surface polarisation, decreasing the band gap in 2D-FeS<sub>2</sub>. The same has been observed in 2D TDMC, and researchers have shown that applying an external transverse field can reduce the band gap that results from the semiconductor-to-metal transition.30 The electric field can alter the chemical potential of electrons, allowing them to delocalise depending on the polarity of the charge applied. This induces an anisotropy in the electronic structure, which breaks the inversion symmetry, leading to spin-orbit (SO) splitting in the valence and conduction band. This effect is called the Giant-Stark Effect (GSE) and describes a phenomenon similar to the standard Stark effect for atomic orbitals. The GSE is based on the fact that transverse electric fields are responsible for mixing electronic states, leading to

a splitting of the electronic bands. The quantum-confined Stark effect (QCSE)<sup>31–34</sup> describes a striking alteration in the energies of quantum states induced by an electric field in low-dimensional materials. By applying the electric field along the confinement direction of a quantum well or other nanostructure, a large electric field can cause a massive shift of exciton states. The energy of the constituent electron states in the conduction bands and the hole states in the valence bands change in opposite directions, causing the band gap to shrink proportionally to the electric field. When an electric field is applied, the wave functions of the electron and hole within the confined structure move in opposite directions, causing the exciton binding energy to be suppressed. In light of this, we investigated the impact of the external electric field on the band structures of 2D-FeS<sub>2</sub>.

Fig. 6(i-k) presents the outcomes of our computational analysis elucidating the band structure of 2D-FeS2 under the influence of external electric field strength of E = 1, 2, and  $3 \text{ V Å}^{-1}$ . The remarkable discovery is that the band gap changes from its original value of 0.241 eV (in the absence of an external electric field) to a state approximating metallic behavior at  $E = 3 \text{ V Å}^{-1}$ . Specifically, the lower conduction band (CB) exhibited a discernible upward shift of 0.01 eV, resulting in a band gap of 0.251 eV when subjected to an electric field of  $E = 1 \text{ V Å}^{-1}$ . Further, with an increased electric field strength of  $E = 2 \text{ V Å}^{-1}$ , the band gap was subsequently reduced to 0.152 eV. Notably, metallic band overlap was observed at  $E = 3 \text{ V Å}^{-1}$ . Notably, electric fields at or below  $E \le 1 \text{ V Å}^{-1}$  led to an upward displacement of the lower conduction band and heightened confinement of available states near the Fermi level. In contrast, electric fields at or exceeding  $E \ge 1 \text{ V Å}^{-1}$  induced an upward displacement of valence bands within excited orbitals, attributed to the Giant-Stark Effect (GSE). Fig. 6l depicts the decrease in the bandgap with an increase in electric field. Similar observations have been made for bilayer TMC, where the bandgap decreases linearly with the electric field.35 Consequently, the application of a stronger electric field has the potential to modulate the band gap significantly.

The impact of GSE on lowering of bandgap can affect the Schottky barrier height at the metal-semiconductor junction. The Schottky barrier height of a p-type semiconductor is defined as

$$\Phi_{\rm B} = (E_{\rm g} + \chi) - \Phi_{\rm M} \tag{3}$$

where  $\Phi_{\rm m}$  the metal work function in eV,  $\chi$  is the electron affinity, and  $E_{\rm g}$  is the bandgap. From the above equation, it is clear that electron affinity increases as the band gap decreases, which in turn lowers the Schottky barrier height.<sup>36</sup> A lower Schottky barrier height will result in a lower built-in potential by the following equation.

$$eV_0 = \Phi_{\rm B} - (E_{\rm c} - E_{\rm F})$$
 (4)

where  $E_{\rm c}$  is the energy of the conduction band, and  $E_{\rm F}$  is the Fermi level. The built-in potential is calculated using the following equation.

$$V_0 = E_{\rm g} + \chi - \Phi_{\rm M} \tag{5}$$

The derived equations indicate a built-in potential of approximately 0.17 V for the device, closely aligned with its turnon voltage obtained from Fig. 3e. Eqn (4) and (5) show that the built-in potential decreases in direct proportion to the Schottky barrier. This suggests that a lower input voltage is sufficient for electrons in the conduction band to overcome the potential barrier and allow current to flow. This relationship directly leads to a lower diode turn-on voltage, which makes the device more sensitive to low-powered RF signals. Experimental studies substantiate this enhancement in sensitivity. We have performed thickness-dependent I-V characteristics as shown in ESI Fig. S4† and observed that as thickness increased, the turn-on voltage was increasing, possibly due to the annihilation of GSE with the thickness of FeS<sub>2</sub> coatings. On the other hand, studies on bulk FeS2 crystals, as shown in ESI Fig. S3,† also indicate inadequate rectification and a high turn-on voltage. These findings justify the unique application of GSE-induced 2D materials for RF applications.

An overview of reported materials for RF energy harvesting is provided in ESI Table 1.† It has been reported that 2D materials with RF energy harvesting properties include MoS2, MoSe2, WSe2, and Si. However, they are synthesised using expensive and time-consuming methods like Atomic Layer Deposition photolithography, electron beam lithography, magnetron sputtering and Plasma-Enhanced Chemical Vapor Deposition techniques. The techniques used require demanding conditions, such as high vacuum, high power, and precision requirements, which make them operationally timeconsuming. Additionally, the utilisation of pristine precursor samples and precious metals like Au and Pt for electrode deposition entails substantial costs. The reliance on the mechanical exfoliation method inherently limits scalability. These materials also require careful handling procedures because they are oxidation-sensitive. Even with all of these complex steps, it is important to note that devices made of these materials have high turn-on voltages, which limits their use to high-power radio functions like switching instead of RF energy harvesting. Furthermore, the environmental impact associated with materials like Se and Pb necessitates the exploration of eco-friendly alternatives. In addressing these challenges, FeS<sub>2</sub> emerges as a promising candidate, being both abundant and eco-friendly. In our research, we employed the conventional liquid phase exfoliation method to synthesise 2D-FeS2, and simple drop-casting techniques at ambient conditions rendered the process cost-effective and time-efficient. The liquid phase exfoliation method represents a remarkable breakthrough in yielding abundant 2D-FeS<sub>2</sub>. Additionally, because it is a p-type semiconductor with a large work function, the choice of electrode materials is extremely broad and includes easily obtained metals like Ti and Al, which makes the fabrication process extremely economical. Moreover, the adaptability of our methodology encompasses the smooth integration of flexible substrates via the simple and useful drop-casting method, augmenting practicability and accessibility. Fig. 7a illustrates the operating frequency range of various reported materials in

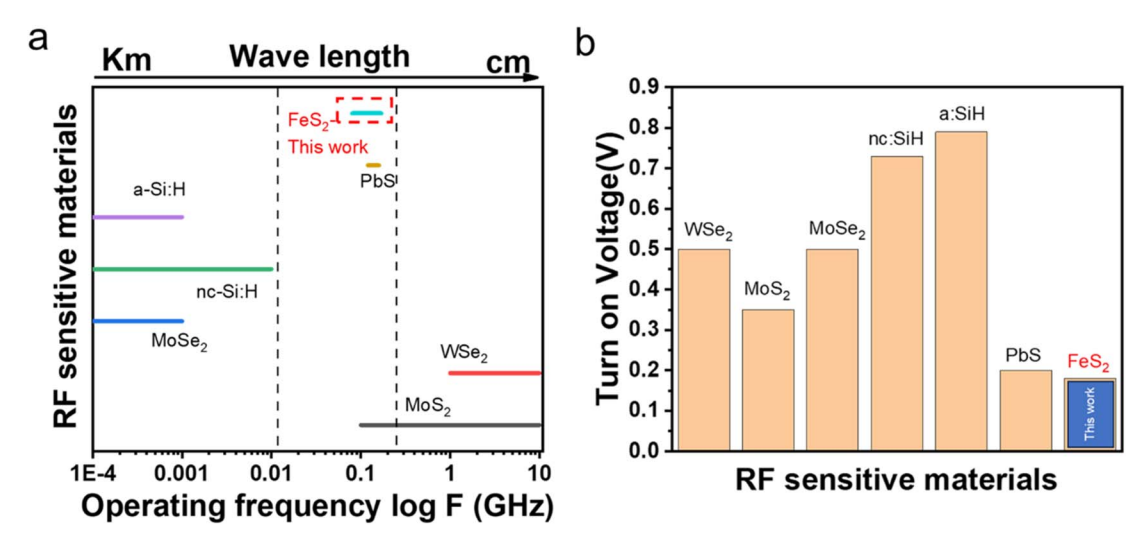


Fig. 7 (a) Operating frequencies of different materials in available RF sources and (b) turn-on voltage of various RF-sensitive materials.

the radio spectrum for RF energy harvesting. For satisfactory reception of radio waves, the antennas of radio receivers should have one-quarter of their wavelength. Materials like a:Si:H, nc:SiH, and MoSe<sub>2</sub> operating in low frequencies will require a larger length antenna for decent reception of RF signals. This limitation poses challenges for their integration into electronic circuits for energy harvesting, particularly for portable devices. In contrast, 2D-FeS2 operates in lower frequency RF bands such as commercial FM broadband and HAM radio bands; the requirement for extensive antennas or additional components like repeaters can be removed. This makes 2D-FeS2 suitable for integration into portable devices such as laptops, computers, and electronic gadgets for RF energy harvesting. Unlike materials like MoS2 and WSe2, which necessitate high-power RF sources, repeaters, and high-gain antennas for effective operation, 2D-FeS2 operates efficiently without such requirements. As shown in Fig. 7b, its lower turn-on voltage is advantageous, allowing the conversion of low-signal RF to useful voltage. Despite the numerous benefits provided by 2D-FeS2, one major limitation is its ability to extend RF sensitivity to higher frequencies. Investigating various metal contacts and the thickness dependencies of 2D-FeS2 on RF sensitivity are useful approaches to take on this challenge. Interestingly, even though 2D-FeS<sub>2</sub> responds in commercial broadband frequencies, its potential uses go well beyond that, including high-frequency field-effect transistors, long-range RF identification sensors, and electromagnetic shielding, among other wireless technologies. In conclusion, using 2D-FeS2 for RF energy harvesting appears to be a significant and affordable way to achieve the goal of a future powered by wireless technology.

#### 3 Experimental section/methods

#### Material synthesis

2D-FeS2 was synthesised using a liquid-phase exfoliation method. 5 g of bulk FeS2 crystals were crushed with a pestle and mortar to obtain powder, and a subsequent 4 hours of

sonication in 100 mL isopropyl alcohol (IPA) solvent followed. The dispersion was allowed to settle for an hour to separate the nanoparticles from the bulk particles. The 2D nanoparticles were then separated from the rest of the dispersion by centrifugation. The 2D nanoparticle dispersion was isolated using a dropper and transferred to sample bottles for further analysis.

#### 3.2 Characterisation

Both bulk and 2D-FeS2 samples were characterised for structural, morphological, spectroscopic, and electronic properties. Phase analysis was done by X-ray diffraction (XRD) (Bruker D8 Advance with a Lynx eye detector using Cu-Kα radiation). The morphology and atomic arrangements were analysed using scanning electron microscopy (SEM) (ZEISS Sigma) and highresolution transmission electron microscopy (HRTEM) (advanced Titan electron microscope). The atomically-thin nature of 2D-FeS2 was confirmed using atomic force microscopy (AFM) (Pico Scan 5100, Agilent Technologies). Vibrational modes were analysed using Raman spectroscopy (WITec, UHTS 300VIS, Germany). The chemical states of 2D-FeS2 were analysed using X-ray photoelectron spectroscopy (XPS) (Thermo Fisher Scientific makes Nexsa base). Current-voltage characteristics were determined using a source meter (Keithley 2450). RF studies were conducted using a lab-made RF setup consisting of an RF generator (35 MHz-4.4 GHz), an RF power amplifier, a standing wave ratio (SWR) power meter, Walkie Talkie (Baofeng UVR5R) and an oscilloscope (Tektronix 1072 B).

#### 3.3 Device fabrication and experimental setup

Radiofrequency (RF) energy harvesting devices can transform RF signals into useable electrical power without a biasing circuit. To fabricate the device, we created a homemade setup that consists of a substrate holder and a metal wire holder that can be adjusted to accommodate different substrate sizes and different kinds of metal contacts. As one of the contact electrodes, we used a commercially available indium tin oxide (ITO) substrate with dimensions of  $1 \times 1 \times 0.7$  cm and drop-cast 2D-FeS $_2$  on it while keeping the substrate temperature at 40 °C. We connected a mechanical titanium electrode of 0.758 mm $^2$  area, which can be moved up and down to adjust the contact height as the working electrode to the 2D-FeS $_2$  coating. A schematic representation of device fabrication using the drop-casting method is given in ESI Fig. S1.† Output connections were taken from the ITO substrate and the Ti electrode. The overall configuration of the device is Ti/2D-FeS $_2$ /ITO.

#### 3.4 Computational methodology

Density functional theory (DFT) simulations were carried out for the FeS<sub>2</sub> structure using the DMol<sup>3</sup> code.<sup>37</sup> We used the initial crystal and atomic coordinates parameters from the experimental XRD analysis for FeS2 bulk. A 2D-FeS2 crystal structure was created by cleaving the (1 0 0) plane from FeS<sub>2</sub> bulk and adding a 15 Å vacuum buffer separation to remove any nonbonding energy interactions perpendicular to the plane. The generalised gradient approximation (GGA) method was used in all simulations using the exchange-correlation functional by Perdew-Burke-Ernzerhof (PBE).38 We used a double numerical (DN) basis set, which includes a minimal basis and a second set of valence atomic orbitals. The self-consistent field (SCF) convergence criterion for electronic optimisations was 10<sup>-6</sup> eV per atom. We used a  $2 \times 2 \times 1$  k-points mesh with all electrons included in the calculation, and the simulation box was allowed to relax during the variable cell calculation.

# 4 Conclusions

In summary, we fabricated an RF energy harvesting Schottky device using a Ti/2D-FeS<sub>2</sub>/ITO configuration by drop casting method. 2D-FeS2 was synthesized from earth-abundant pyrite ore through a liquid phase exfoliation technique. The microscopic and spectroscopic studies confirmed the stability of 2D-FeS<sub>2</sub>. Electrical studies revealed that the device made of 25 μm film of 2D-FeS2 has a low turn-on voltage of 0.18 V and a low Schottky barrier height of 0.16 eV. The role of 2D-FeS2 on the electronic properties of the device was analyzed using density functional theory studies which revealed the contribution of the Giant Stark Effect in 2D-FeS2. This shed light on the impact of lowering the band gap from bulk FeS2 to 2D-FeS2 which resulted in a possible lowering of turn on voltage of the device. This satisfied the criteria for the device to behave as an ideal RF energy harvesting device since a low turn-on RF voltage will be sufficient to turn on the diode. After confirming this, we proceeded with RF studies of the device in commercial FM broadband (88-108 MHz) and very high-frequency band (130-170 MHz) because of its easy availability in the ambient conditions. Experimental studies revealed that the device has an overall efficiency of 30% which can be improved by adding additional network-matching circuits to the device. Theoretical studies revealed the effect of external electric field in lowering the bandgap of 2D-FeS<sub>2</sub> suggesting possible future applications in field effect transistors for high-speed applications. The obtained experimental and theoretical studies show that RF

energy harvesting using earth-abundant FeS<sub>2</sub> serves as a potential candidate for sustainable energy harvesting.

# **Author contributions**

Karthik R.: conceptualization, methodology, investigation, writing – original draft, visualization, Appu Kumar Singh: software, formal analysis, Shreyasi Das: validation, investigation, Suman Sarkar: resources, Tarun Kumar Kundu: writing – review & editing, Swastik Kar: writing – review & editing, P. R. Sreeram: conceptualization, writing – original draft, writing – review & editing, supervision, Chandra Sekhar Tiwary: resources, writing – review & editing, supervision, project administration, funding acquisition.

# Conflicts of interest

There are no conflicts to declare.

# Acknowledgements

SK acknowledges support provided by the National Science Foundation through the ExpandQISE award no. 2329067 and the Massachusetts Technology Collaborative through award number 22032. CST acknowledges the Core Research Grant of SERB, India, the STAR project by MHRD-India, the DAE Young Scientist Research Award (DAEYSRA), and AOARD (Asian Office of Aerospace Research and Development) (grant nos. FA2386-21-1-4014 and FA2386-23-1-4034).

### Notes and references

- 1 L.-G. Tran, H.-K. Cha and W.-T. Park, *Micro Nano Syst. Lett.*, 2017, 5, 14.
- 2 Y.-H. Suh and K. Chang, *IEEE Trans. Microw. Theory Tech.*, 2002, **50**, 1784–1789.
- 3 K. Rajeev, S. Punathil Raman, A. Kumar Singh, M. R. Anantharaman, S. Abraham Sam, S. Sarkar, T. Kumar Kundu and C. Sekhar Tiwary, *ACS Appl. Nano Mater.*, 2023, **6**, 10168–10177.
- 4 P. Kumbhakar, J. S. Jayan, A. Sreedevi Madhavikutty, P. R. Sreeram, A. Saritha, T. Ito and C. S. Tiwary, *iScience*, 2023, **26**, 106671.
- 5 T. Chowdhury, E. C. Sadler and T. J. Kempa, *Chem. Rev.*, 2020, **120**, 12563–12591.
- 6 M. B. Tahir and U. Fatima, Energy Storage, 2022, 4, e244.
- 7 J. E. ten Elshof, H. Yuan and P. Gonzalez Rodriguez, *Adv. Energy Mater.*, 2016, **6**, 1600355.
- 8 C. Cui, F. Xue, W.-J. Hu and L.-J. Li, npj 2D Mater. Appl., 2018, 2, 18.
- 9 H. Kim and H. J. Choi, *Phys. Rev. B*, 2021, **103**, 085404.
- 10 X. Zhang, J. Grajal, J. L. Vazquez-Roy, U. Radhakrishna, X. Wang, W. Chern, L. Zhou, Y. Lin, P.-C. Shen, X. Ji, X. Ling, A. Zubair, Y. Zhang, H. Wang, M. Dubey, J. Kong, M. Dresselhaus and T. Palacios, *Nature*, 2019, 566, 368–372.
- 11 S. J. Yang, K.-T. Park, J. Im, S. Hong, Y. Lee, B.-W. Min, K. Kim and S. Im, *Nat. Commun.*, 2020, 11, 1574.

- 12 L. J. Widiapradja, S. Hong, K.-T. Kim, H. Bae and S. Im, Nano Energy, 2022, 92, 106771.
- 13 K. Rajeev, A. K. Singh, P. R. Sreeram, P. L. Mahapatra, D. S. Galvao and C. S. Tiwary, Nanoscale, 2023, 15, 9022-
- 14 J. Zhang, Y. Li, B. Zhang, H. Wang, Q. Xin and A. Song, Nat. Commun., 2015, 6, 7561.
- 15 H. Wang, C.-H. Li, Y. Liu, S. D. Joseph, Y. Huang and S. S. H. Hsu, Jpn. J. Appl. Phys., 2020, 59, SGGD12.
- 16 B. Hyde and M. Okeeffe, Aust. J. Chem., 1996, 49, 867.
- 17 C. Steinhagen, T. B. Harvey, C. J. Stolle, J. Harris and B. A. Korgel, J. Phys. Chem. Lett., 2012, 3, 2352-2356.
- 18 H. Kaur, R. Tian, A. Roy, M. McCrystall, D. V. Horvath, G. Lozano Onrubia, R. Smith, M. Ruether, A. Griffin, C. Backes, V. Nicolosi and J. N. Coleman, ACS Nano, 2020, 14, 13418-13432.
- 19 I. Mondal, S. Y. Moon, H. Lee, H. Kim and J. Y. Park, J. Mater. Chem. A, 2019, 7, 19258-19268.
- 20 A. Kirkeminde, B. A. Ruzicka, R. Wang, S. Puna, H. Zhao and S. Ren, ACS Appl. Mater. Interfaces, 2012, 4, 1174-1177.
- 21 J. Zhou, L. Shen, M. D. Costa, K. A. Persson, S. P. Ong, P. Huck, Y. Lu, X. Ma, Y. Chen, H. Tang and Y. P. Feng, Sci. Data, 2019, 6, 86.
- 22 M. Ishigami, J. D. Sau, S. Aloni, M. L. Cohen and A. Zettl, Phys. Rev. Lett., 2005, 94, 056804.
- 23 B. Yuan, W. Luan and S. Tu, Dalton Trans., 2012, 41, 772-776.
- 24 M. Y. C. Teo, S. A. Kulinich, O. A. Plaksin and A. L. Zhu, J. Phys. Chem. A, 2010, 114, 4173-4180.

- 25 L. Li, P. Ma, S. Hussain, L. Jia, D. Lin, X. Yin, Y. Lin, Z. Cheng and L. Wang, Sustainable Energy Fuels, 2019, 3, 1749-1756.
- 26 S. Yang, X. Song, P. Zhang, J. Sun and L. Gao, Small, 2014, 10, 2270-2279.
- 27 K. P. Bhandari, R. R. Khanal, N. R. Paudel, P. Koirala, P. J. Roland, T. Kinner, Y. Yan, R. W. Collins, M. J. Heben and R. J. Ellingson, in 2014 IEEE 40th Photovoltaic Specialist Conference (PVSC), IEEE, 2014, pp. 2293–2298.
- 28 O. Hübner and J. Sauer, Phys. Chem. Chem. Phys., 2002, 4, 5234-5243.
- 29 Z. Xiaoling, L. Fei, L. Changzhi, X. Xuesong, L. Ying and S. N. Mohammad, J. Semicond., 2009, 30, 034001.
- 30 A. Ramasubramaniam, D. Naveh and E. Towe, Phys. Rev. B: Condens. Matter Mater. Phys., 2011, 84, 205325.
- 31 C. Chakraborty, K. M. Goodfellow, S. Dhara, A. Yoshimura, V. Meunier and A. N. Vamivakas, Nano Lett., 2017, 17, 2253-2258.
- 32 M. Ishigami, J. D. Sau, S. Aloni, M. L. Cohen and A. Zettl, Phys. Rev. Lett., 2005, 94, 56804.
- 33 X. Lu and L. Yang, Appl. Phys. Lett., 2017, 111, 193104.
- 34 S. Haastrup, S. Latini, K. Bolotin and K. S. Thygesen, Phys. Rev. B, 2016, 94, 41401.
- 35 A. Kuc and T. Heine, Chem. Soc. Rev., 2015, 44, 2603-2614.
- 36 P. K. Baumann, S. P. Bozeman, B. L. Ward and R. J. Nemanich, Diamond Relat. Mater., 1997, 6, 398-402.
- 37 B. Delley, J. Chem. Phys., 2000, 113, 7756-7764.
- 38 J. P. Perdew, K. Burke and M. Ernzerhof, Phys. Rev. Lett., 1996, 77, 3865-3868.